

Preparation and Lithium Storage Properties of MOF-Derived Bimetallic Sulfide $Zn_xIn_yS/MXene$ Composites

Yinghui Xue^{†,*[a]} Wanjiao Li^{†,[a,b]} Runrun Liu,^[a] Tong Zhao,^[a] Yuepeng Lv,^[a] Jianxin Li,^[a] Yao Guo,^[a] Rui Hao,^{*[b]} Xijun Liu,^[c] and Huibing He^{*[c]}

Nanostructured metal sulfides (MSs) are considered promising anode materials for Li-ion batteries (LIBs) due to their high specific capacity and abundant raw material resources. However, the practical application of these materials faces challenges such as poor conductivity and volume expansion. To address these issues and enhance the performance of LIBs, it is crucial to tackle the structural design problem associated with Zn_xIn_yS anode material. The utilization of metal sulfides derived from metal-organic frameworks (MOFs) not only improves conductivity but also mitigates the issue of volume expansion in metal sulfides. Furthermore, connecting the metal sulfides derived from MOF to various conductive substrates can further enhance their conductivity. Two-dimensional transition metal

carbides and nitrides (MXenes), a novel type of 2D material with plentiful functional groups and chemical properties, offer great potential. In this study, we have strategically constructed $Zn_xIn_yS/MXene$ heterostructures by combining the advantages of 2D $Ti_3C_2T_x$ nanosheets and bimetallic MOF structures. The results demonstrate that due to the synergistic effect between MXene and heterostructure, a significant number of lattice defects and ample buffer space are provided, resulting in excellent lithium storage performance and fast ion diffusion kinetics for the electrode. In cyclic performance tests conducted at a current density of $0.5 \text{ A} \cdot \text{g}^{-1}$, an outstanding lithium storage capacity of $1300 \text{ mAh} \cdot \text{g}^{-1}$ was achieved after 450 cycles.

Introduction

In today's society, the efficiency of energy storage and conversion is directly correlated with the sustainable development of the global economy. LIBs have emerged as the predominant technology in the portable electronics market owing to their exceptional operational voltage, high energy density, minimal self-discharge rate, and extended cycle life.^[1,2] Owing to the extensive application in electric vehicles and large-scale power grids, the demand for lithium-ion batteries (LIBs) with enhanced energy density, safety, and stability is continuously increasing.^[3] The electrode material plays a crucial role in the performance of LIBs.^[4–6] Existing cathode materials

such as LiFePO_4 , LiMn_2O_4 , and LiCoO_2 have reached a relatively mature stage and are widely utilized in various applications.^[7–10] However, the commercial anode material is mainly graphite, which has the advantages of abundant resources and low cost, but its theoretical capacity is relatively low ($372 \text{ mAh} \cdot \text{g}^{-1}$),^[11] its rate performance is poor, and it is easy to form lithium dendrite at low working potential. Developing high-performance new anode materials is crucial for further enhancing the performance of lithium-ion batteries.^[12]

Metal sulfides exhibit advantages such as high specific capacity, excellent mechanical properties, and low cost. They possess weak metal-sulfur bonds that are more prone to breaking during the Li^+ conversion reaction, thereby enhancing electronic conductivity and demonstrating rapid reaction kinetics.^[13,14] As a bimetallic sulfide, Zn_xIn_yS features an extended atomic connectivity and complex material structure, which facilitates a wider range of redox reactions, higher electrochemical activity, and superior electronic conductivity.^[15–20] For instance, Zhang^[21] successfully synthesized a core-shell structured $\text{Sb}_2\text{S}_3/\text{MoS}_2$ composite material by hydrothermally depositing molybdenum sulfide nanosheets onto antimony sulfide nanorods. Compared with single metal sulfides, this core-shell structure exhibits enhanced cycling stability. However, during the reaction process of bimetallic sulfides, volume expansion occurs, leading to a rapid decline in capacity. To address these issues, various strategies have been employed, including carbon coating and structural modifications.^[22] For example, Guo et al. improved energy storage performance through carbon coating on nanomaterials,^[23] while Mok et al. utilized dopamine-derived carbon shells to enhance the lithium storage performance of CoMoS .^[24]

[a] Dr. Y. Xue,[†] W. Li,[†] R. Liu, T. Zhao, Dr. Y. Lv, Dr. J. Li, Dr. Y. Guo
School of Materials Science and Engineering
Anyang Institute of Technology
Huanghe Avenue West Section, Anyang, China
E-mail: xueyh@ayit.edu.cn

[b] W. Li,[†] Dr. R. Hao
Henan Key Laboratory of Coal Green Conversion, Henan International Joint Laboratory of Coal Clean Utilization, College of Chemistry and Chemical Engineering
Henan Polytechnic University
No. 142, Middle Jiefang Road, Jiaozuo, China
E-mail: haorui@hpu.edu.cn

[c] Prof. X. Liu, Dr. H. He
School of Chemistry and Chemical Engineering
Guangxi University
No. 100, East University Road, Nanning, China
E-mail: huibinghe@gxu.edu.cn

[†] These authors contributed equally to this work.

Supporting information for this article is available on the WWW under
<https://doi.org/10.1002/batt.202400770>

This paper aims to alleviate volume expansion and enhance battery capacity by combining metal-organic frameworks (MOFs) with MXene. Compared to conventional synthesis methods for metal sulfides, materials derived from metal-organic frameworks (MOFs) retain the structural, compositional, and porous characteristics of MOFs.^[25–28] The ordered pore structure of MOFs can not only promote efficient electrolyte penetration and ion diffusion but also increase lithium-ion migration through unsaturated metal sites (UMS) or positively/negatively charged functional groups.^[29] MXenes, as a new class of two-dimensional transition metal carbides, nitrides, or carbonitrides.^[30–34] exhibit effective synergies with MOFs to mitigate volume expansion and improve the electrochemical performance of batteries. Their layered structures provide conductive networks for rapid charge transfer and sufficient electrolyte penetration. Additionally, strong interfacial interactions between metal sulfides and MXene significantly enhance the kinetics of ion or electron transfer and offer additional interfacial active sites to boost electrode capacity.^[35] MXene@-MOF composites can be synthesized via in-situ methods or simple mixing techniques. Moreover, using MOFs or MXenes as sacrificial templates allows for the preparation of derivatives within the MXene@MOF system.

We proposed an ingeniously designed Zn_xIn_yS/MXene heterostructure, effectively integrating the advantages provided by 2D Ti₃C₂T_x nanosheets and BMOF. Through the one-step synthesis method using BMOF precursors, we successfully prepared MOF-derived sulfide/MXene composites via hydrothermal sulfidation. The lithium storage performance of the synthesized Zn_xIn_yS/MXene composites surpasses that of single

Zn_xIn_yS. At a current density of 1 A·g⁻¹, after 1000 cycles, its discharge capacity reaches 1097 mAh·g⁻¹. Furthermore, the heterogeneous structure significantly lowers the energy barrier for ion diffusion, thereby accelerating transmission rates and enhancing ion storage capacity.^[36] Consequently, even at a high current density of 5 A·g⁻¹, a remarkably high reversible capacity is maintained.

Results and Discussion

Firstly, the structure and composition of the samples were analyzed using X-ray diffraction (XRD). Figure 1a depicts the XRD patterns of Zn_xIn_yS/MXene, MXene, and Zn_xIn_yS. The XRD pattern of Zn_xIn_yS/MXene exhibits three distinct diffraction peaks at 27.4°, 32.3°, and 47.6°, corresponding to the crystal planes (109) and (208) of In₂S₃, as well as the crystal plane (110) of ZnS. The XRD patterns of Zn_xIn_yS/MXene exhibit a remarkable resemblance to those of Zn_xIn_yS. Notably, for the hydrothermal vulcanization-synthesized Zn_xIn_yS/MXene at 140 °C, an amorphous nature is indicated by a broad peak observed between 25° and 30°. In comparison with the Zn_xIn_yS sample, Zn_xIn_yS/MXene displays a broader diffraction peak with lower intensity, suggesting inferior crystallinity in the prepared sample.

We investigated the surface chemical state of the Zn_xIn_yS/MXene composite material using XPS. The C1s spectrum (Figure 1b) exhibits four distinct peaks: the C-Ti peak at 284.3 eV, the C-C peak at 285.0 eV, the C-O peak at 286.0 eV, and the C=O peak at 288.5 eV.^[37] The presence of the C-Ti peak confirms the existence of MXene in the composite. Figure 1c

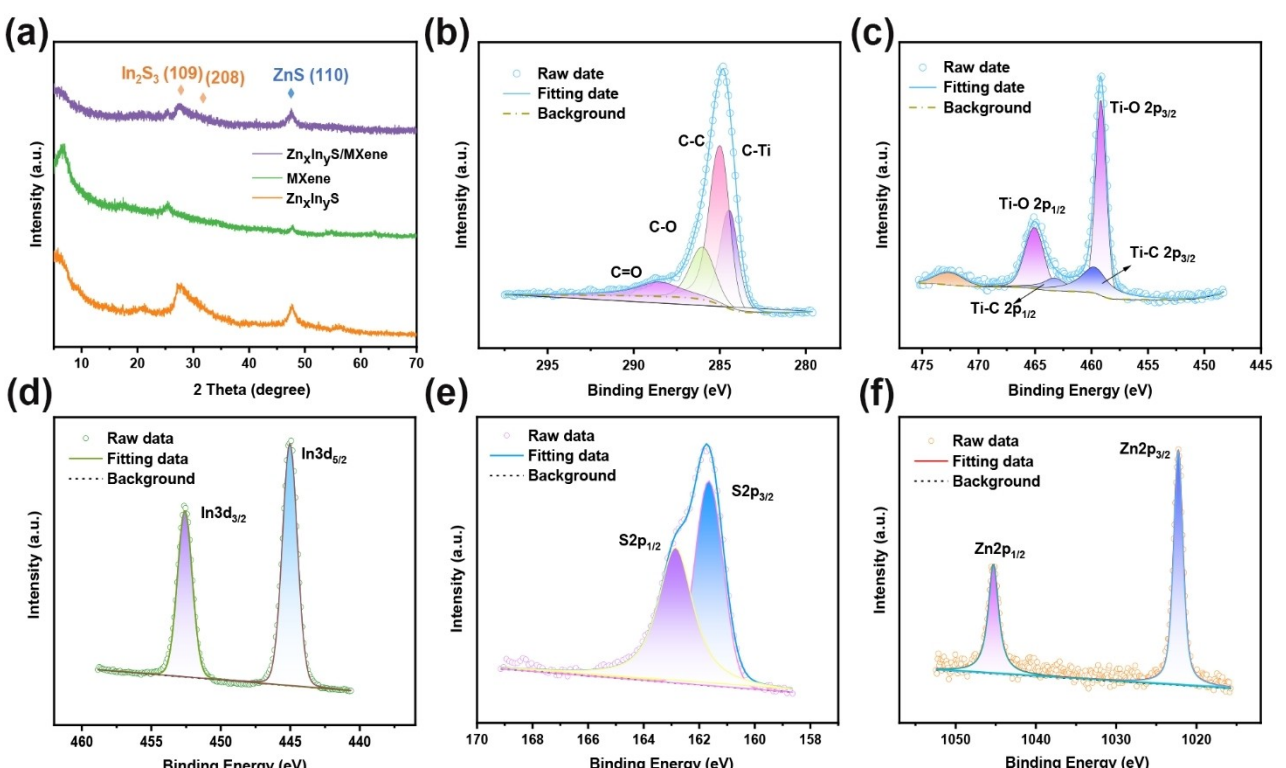


Figure 1. a) XRD pattern of Zn_xIn_yS/MXene, MXene and Zn_xIn_yS. b, c, d, e, f) The XPS spectrum of C1s, Ti 2p, In 3d, S 2p and Zn 2p.

shows the high-resolution Ti 2p spectrum, which reveals Ti–O 2p_{3/2} (459.17 eV), Ti–O 2p_{1/2} (465.05 eV), Ti–C 2p_{3/2} (459.71 eV), and Ti–C 2p_{1/2} (463.27 eV).^[38] The Ti–O peaks at 459.17 eV and 465.05 eV are attributed to the oxidation of MXene during the hydrothermal process and the oxygen-containing functional groups on its surface.^[39] Figure 1d presents the high-resolution In3d spectrum, displaying a pair of symmetrical peaks at 445.0 eV and 452.6 eV, corresponding to In3d_{5/2} and In3d_{3/2}, respectively.^[40] Additionally, the high-resolution XPS spectrum of S2p exhibits two distinct peaks at 161.6 eV and 162.8 eV. Two distinct Zn peaks are observed in Figure 1f, with binding energies of 1022.2 eV and 1045.3 eV, corresponding to Zn 2p_{3/2} and Zn 2p_{1/2}, respectively.^[41] Among them, the atomic ratio of In to Zn is approximately 4.5 to 1. These results confirm that the Zn_xIn_yS/MXene composite material was successfully synthesized via hydrothermal sulfidation.

The scanning electron microscopy (SEM) images in Figure 2a depict the Zn-MIL-68 (In) MOF, where the precursor retains its hexagonal rod structure. The average size of nanorods has increased from 8–10 μm to 12–14 μm. It is speculated that the presence of Zn²⁺ promotes axial growth of the rod-like structure. Figure 2b shows SEM images of Zn_xIn_yS, wherein vulcanization results in a roughened surface for the bimetallic sulfide with a rod-shaped morphology. The Zn_xIn_yS/MXene composites, as depicted in Figure 2c, consist of stacked layers of Zn_xIn_yS and MXene. To further investigate the microstructure of Zn_xIn_yS/MXene, transmission electron microscopy (TEM) analysis was conducted. The TEM image in Figure 2d and 2e

clearly depicts the well-defined nanotubular architecture and carbon layer of the Zn_xIn_yS/MXene product, exhibiting an average size range of 500–600 nm for the formed nanotubes. The high-resolution TEM image in Figure 2f reveals a stripe spacing of 0.28 nm, which corresponds to the (208) crystal plane of In₂S₃. Similarly, the stripe spacing of 0.20 nm corresponds to the (110) crystal plane of ZnS. The observed electron selected area of electron diffraction (SAED) pattern in Figure 2g exhibits well-matched diffraction rings corresponding to the crystal planes of In₂S₃ (109), (208), and ZnS (110). We conducted an in-depth analysis of the EDS spectra of individual nanotubes. As illustrated in Figure 2h–2l, the elements In, Zn, Ti, C, and S exhibit uniform distribution throughout the structure, which is in agreement with the XPS findings.

The cyclic voltammetry (CV) plot of Zn_xIn_yS/MXene at a scanning speed of 0.1 mVs⁻¹ is presented in Figure 3a. It is important to highlight that the CV curve of the initial cycle exhibits distinct differences from subsequent cycles, particularly during the discharge phase. In the first anodic scan, three reduction peaks were observed at 0.67 V, 1.24 V, and 1.7 V, corresponding to the oxidation reactions of In and Zn. This was followed by a prominent oxidation peak near 0.9 V, indicative of reduction reactions (In³⁺ to In, Zn²⁺ to Zn). During the second scan, the oxidation peak at 0.9 V shifted to approximately 1.1 V, while the positions of the reduction peaks remained largely unchanged, suggesting the activation process of the MXene/Zn_xIn_yS MOF anode.^[42] In the third scan, the CV curve remained almost identical, with only a slight decrease in peak current

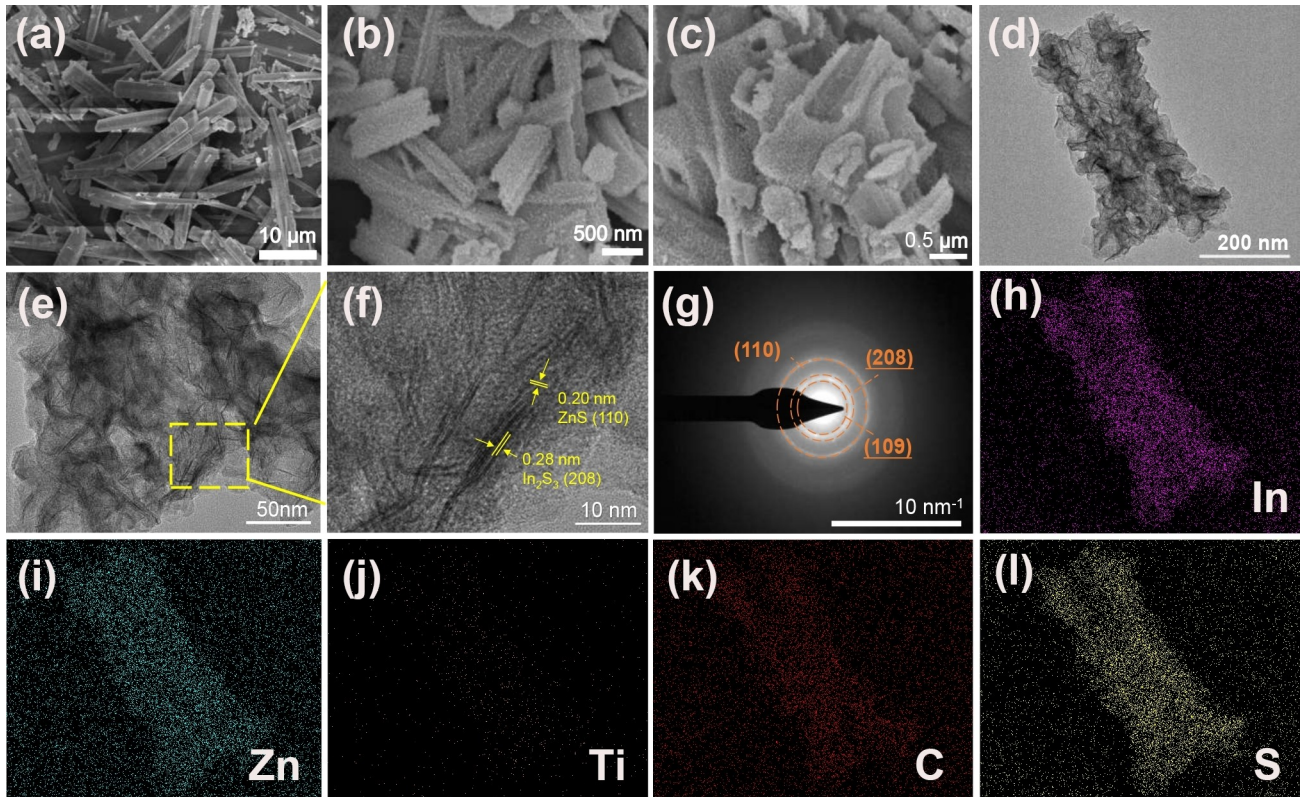


Figure 2. a) bimetallic Zn-MIL-68(In) MOF. b) Zn_xIn_yS. c) Zn_xIn_yS/MXene Composites. d, e) TEM image of Zn_xIn_yS/MXene composite material. f) HRTEM image of Zn_xIn_yS/Mxene. g) SAED image of Zn_xIn_yS/Mxene. h, i, j, k, l) EDS mapping of Zn_xIn_yS/MXene Composites.

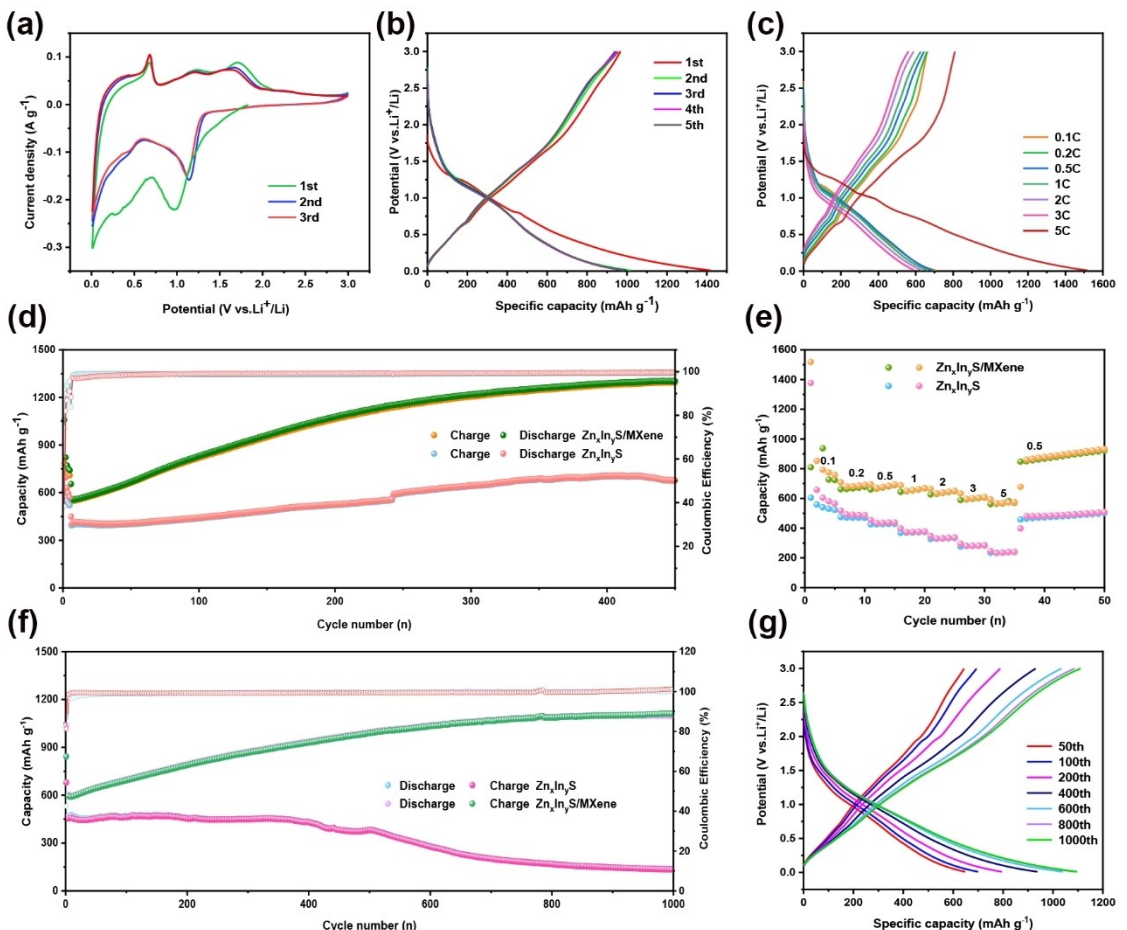


Figure 3. a) The lithium storage performance. CV curves of $\text{Zn}_x\text{In}_y\text{S}/\text{MXene}$ at the first three cycles at a scan rate of $0.1 \text{ mV} \cdot \text{s}^{-1}$. b) Galvanostatic charge-discharge curves at $50 \text{ mA} \cdot \text{g}^{-1}$. c) Galvanostatic charge-discharge curves of $\text{Zn}_x\text{In}_y\text{S}/\text{MXene}$ at different current densities. d) The cycling performance of $\text{Zn}_x\text{In}_y\text{S}/\text{MXene}$ and $\text{Zn}_x\text{In}_y\text{S}$ at $0.5 \text{ A} \cdot \text{g}^{-1}$. e) Rate performance of $\text{Zn}_x\text{In}_y\text{S}/\text{MXene}$ and $\text{Zn}_x\text{In}_y\text{S}$. f) Long term cycling performance of $\text{Zn}_x\text{In}_y\text{S}/\text{MXene}$ and $\text{Zn}_x\text{In}_y\text{S}$ at $1 \text{ A} \cdot \text{g}^{-1}$. g) Galvanostatic charge-discharge curves of $\text{Zn}_x\text{In}_y\text{S}/\text{MXene}$ at different cycles at $1 \text{ A} \cdot \text{g}^{-1}$.

intensity, indicating the excellent electrochemical and structural stability of the MXene/ $\text{Zn}_x\text{In}_y\text{S}$ MOF heterostructure anode.

The charge-discharge curve of the $\text{Zn}_x\text{In}_y\text{S}/\text{MXene}$ electrode at a current density of $50 \text{ mA} \cdot \text{g}^{-1}$ is illustrated in Figure 3b. The initial charge and discharge capacities were measured as 1418.53 and $967.38 \text{ mAh} \cdot \text{g}^{-1}$, respectively, resulting in an initial coulombic efficiency (ICE) of 68.2% . This high capacity and low coulombic efficiency can be attributed to the irreversible formation of the solid SEI film on the electrode surface and electrolyte decomposition. However, after five cycles, the coulombic efficiency significantly increased to reach 97% , indicating excellent reversibility in the reaction between $\text{Zn}_x\text{In}_y\text{S}/\text{MXene}$ and Li^+ . The lithium storage performance of $\text{Zn}_x\text{In}_y\text{S}/\text{MXene}$ material was further evaluated through tests conducted for a total of 450 cycles at a current density of $500 \text{ mAh} \cdot \text{g}^{-1}$. As shown in Figure 3d, while both $\text{Zn}_x\text{In}_y\text{S}/\text{MXene}$ and $\text{Zn}_x\text{In}_y\text{S}$ exhibited similar initial discharge capacities, only $\text{Zn}_x\text{In}_y\text{S}$ demonstrated an initial coulombic efficiency as low as 38.3% , which can be attributed to excessive side reactions during its first discharge process. As the number of cycles increases, the capacity of the $\text{Zn}_x\text{In}_y\text{S}/\text{MXene}$ electrode clearly demonstrates its superior electrochemical performance over $\text{Zn}_x\text{In}_y\text{S}$. The

continuous increase in capacity can be attributed to two factors: The pulverization of $\text{Zn}_x\text{In}_y\text{S}$ /MXene nanoparticles during repeated cycling increases the surface area of the electrode, thereby releasing more active sites for lithium storage; The reversible growth of a polymer gel-like film, caused by the dynamic activation of electrolyte degradation, is common for many metal oxide/sulfide electrodes.^[43] Additionally, analysis of Coulombic efficiency (CE) confirmed the stable behavior of the solid electrolyte interphase (SEI) film throughout cycling, with CE values consistently exceeding 99% . This indicates excellent reversibility for Li^+ ions during shuttle processes.

The rate performance of the negative electrode material was also evaluated, as shown in Figure 3e. It is evident that $\text{Zn}_x\text{In}_y\text{S}/\text{MXene}$ exhibited high discharge capacities at various current densities: $1517.5 \text{ mAh} \cdot \text{g}^{-1}$ ($0.1 \text{ A} \cdot \text{g}^{-1}$), $707.5 \text{ mAh} \cdot \text{g}^{-1}$ ($0.2 \text{ A} \cdot \text{g}^{-1}$), $695 \text{ mAh} \cdot \text{g}^{-1}$ ($0.5 \text{ A} \cdot \text{g}^{-1}$), $688.3 \text{ mAh} \cdot \text{g}^{-1}$ ($1 \text{ A} \cdot \text{g}^{-1}$), $663.6 \text{ mAh} \cdot \text{g}^{-1}$ ($2 \text{ A} \cdot \text{g}^{-1}$), $633 \text{ mAh} \cdot \text{g}^{-1}$ ($3 \text{ A} \cdot \text{g}^{-1}$), and $593.2 \text{ mAh} \cdot \text{g}^{-1}$ ($5 \text{ A} \cdot \text{g}^{-1}$). Notably, even at a higher current density of $5 \text{ A} \cdot \text{g}^{-1}$, the composite demonstrated a reversible capacity of $561.6 \text{ mAh} \cdot \text{g}^{-1}$, surpassing that of $\text{Zn}_x\text{In}_y\text{S}$ significantly. Furthermore, upon returning to a lower current density of $0.5 \text{ A} \cdot \text{g}^{-1}$, the capacity could be restored and remained

stable throughout subsequent cycles. To evaluate its long-term cycling stability, we conducted tests for up to 1000 cycles at a current density of $1 \text{ A} \cdot \text{g}^{-1}$, as shown in Figure 3f. Remarkably, $\text{Zn}_x\text{In}_y\text{S}/\text{MXene}$ exhibited outstanding cycle stability, maintaining a discharge capacity of $1097 \text{ mAh} \cdot \text{g}^{-1}$ even after extensive cycling experiments. In Comparison to $\text{Zn}_x\text{In}_y\text{S}$ counterparts, $\text{Zn}_x\text{In}_y\text{S}/\text{MXene}$ demonstrates superior electrochemical performance, especially under high current densities, due to the conductive substrate of MXene that provides enhanced conductivity and unique mechanical stability.

Due to the excellent rate performance and long-term stability of the $\text{Zn}_x\text{In}_y\text{S}/\text{MXene}$ electrode, we conducted a series of CV tests to further investigate its exceptional electrochemical kinetics source. As depicted in Figure 4a, despite an increase in scanning rate, there is only a slight change in peak area while the CV curve maintains a consistent and favorable shape, indicating good cycle reversibility of the anode. The cathode peak corresponds to Li^+ embedded in $\text{Zn}_x\text{In}_y\text{S}$, whereas the anode peak corresponds to Li^+ detached from $\text{Zn}_x\text{In}_y\text{S}$. It can be observed from the redox peaks that lithiation and delithiation reactions on the electrode remain unchanged at different scanning rates. By analyzing the correlation between scanning rate (v) and recording current (i) at different rates, it is possible to qualitatively verify how capacitance on the electrode surface contributes to overall storage capacity. In summary, this relationship can be expressed as follows:

$$i = av^b \quad (3-1)$$

The Equation (1) defines the proportional constant a , the index b used to evaluate the electrochemical process nature, the scanning rate v , and the peak current i at a specific potential. A value of b close to 0.5 indicates charge storage dominated by hindered ion migration caused by the diffusion coefficient and concentration gradient of the electrode material. When b exceeds 1.0, charge storage is primarily governed by pseudo capacitance. For values between 0.5~1, both diffusion and pseudo capacitance significantly contribute to surface charge storage. As illustrated in Figure 4c, $\text{Zn}_x\text{In}_y\text{S}/\text{MXene}$ demonstrates an anode and cathode peak with a b value of 0.74, indicating rapid reaction kinetics for charge-discharge processes of this material. Furthermore, the contribution of pseudo capacitance can be calculated using the following formula:

$$i = k_1v + k_2v^{1/2} \quad (3-2)$$

The constants k_1 and k_2 represent the coefficients of potential, while k_1v and $k_2v^{1/2}$ denote the contributions of pseudocapacitance and diffusion, respectively.

The pseudo capacitance contribution ratio of $\text{Zn}_x\text{In}_y\text{S}/\text{MXene}$ increases from 46% to 73% as the scanning rate is increased

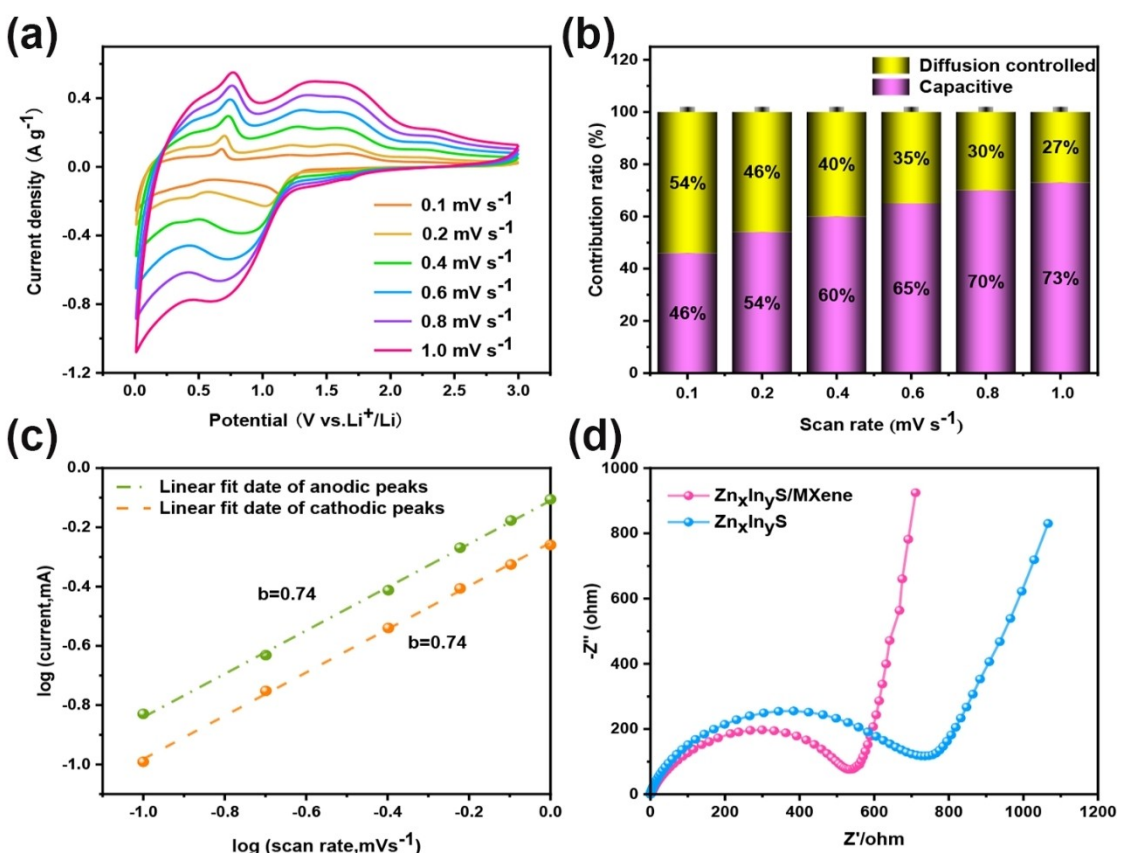


Figure 4. a) CV curves of $\text{Zn}_x\text{In}_y\text{S}/\text{MXene}$ at the scan rates of $0.1\sim1.0 \text{ mV} \cdot \text{s}^{-1}$. b) The ratio of capacitive contribution at different scan rates of $\text{Zn}_x\text{In}_y\text{S}/\text{MXene}$. c) Logarithm peak current and scan rate at anodic and cathodic states. d) AC impedance spectra of $\text{Zn}_x\text{In}_y\text{S}/\text{MXene}$ and $\text{Zn}_x\text{In}_y\text{S}$.

from 0.1 mVs^{-1} to 1 mVs^{-1} , as illustrated in Figure 4b, demonstrating its exceptional rate performance. Electrochemical impedance spectroscopy (EIS) offers a quantitative analysis of the influence of the $\text{Zn}_x\text{In}_y\text{S}/\text{MXene}$ interface state on internal charge transfer efficiency and Li^+ diffusion rate, as depicted in Figure 4d. The impedance curve comprises a semicircle and a slash, where the diameter of the semicircle represents the resistance encountered by Li^+ conduction, while the slash indicates the resistance faced by Li^+ diffusion into the electrode material. The charge transfer resistance (R_{ct}) for $\text{Zn}_x\text{In}_y\text{S}/\text{MXene}$ is slightly lower at 450.2Ω compared to that of $\text{Zn}_x\text{In}_y\text{S}$ at 643.7Ω , further confirming its exceptional electrochemical performance. The remarkable electrochemical properties exhibited by $\text{Zn}_x\text{In}_y\text{S}/\text{MXene}$ can be attributed to its porous structures providing rapid ion and electron transport pathways, as well as synergistic effects arising from heterostructures.

Conclusions

The $\text{Zn}_x\text{In}_y\text{S}/\text{MXene}$ heterostructure was successfully fabricated in this study by synergistically harnessing the merits of 2D $\text{Ti}_3\text{C}_2\text{Tx}$ nanosheets and a BMOF architecture. By tailoring a zinc indium-based BMOF, we effectively enhanced the population of active metal sites compared to single-metal MOFs. Through facile one-pot synthesis of bimetallic MOF precursors, we achieved the formation of sulfide/MXene composites derived from MOFs via hydrothermal vulcanization. The synthesized $\text{Zn}_x\text{In}_y\text{S}/\text{MXene}$ composite demonstrates superior lithium storage performance compared to single $\text{Zn}_x\text{In}_y\text{S}$. Our results illustrate that the $\text{Zn}_x\text{In}_y\text{S}/\text{MXene}$ nanotube, serving as a negative electrode, achieves an impressive lithium storage capacity of $1300 \text{ mAh}\cdot\text{g}^{-1}$ after 450 cycles at a current density of $0.5 \text{ A}\cdot\text{g}^{-1}$. Furthermore, at a current density of $1 \text{ A}\cdot\text{g}^{-1}$, the composite maintains a discharge capacity of $1097 \text{ mAh}\cdot\text{g}^{-1}$ after 1000 cycles while also exhibiting high reversible capacity at a current density of $5 \text{ A}\cdot\text{g}^{-1}$.

Acknowledgements

This work was supported by the Science and Technology Project of Henan Province (No. 242102240085), the Postgraduate Education Reform and Quality Improvement Project of Henan Province (No. YJS2023JD60), the Anyang Institute of Technology, Anyang, Henan, Specialized Research Fund for the Doctoral (No. BSJ2021022), the Key Research Project of Henan Provincial Higher Education (Grant No. 24A430001 and 22B140001), and the Science and Technology Project of Anyang (Grant No. 2023C01GX016).

Conflict of Interests

The authors declare that they have no known competing financial interests or personal relationships that could have appeared to influence the work reported in this paper.

Data Availability Statement

The data that support the findings of this study are available from the corresponding author upon reasonable request.

Keywords: bimetallic sulfide · Metal-organic frameworks · Lithium storage · Mxenes · heterostructure

- [1] R. Amal, H. Zhao, D. Wang, L. Wang, *Vol. 7*, Wiley Online Library, 2017, p. 1703091.
- [2] J. Theerthagiri, S. J. Lee, P. Shanmugam, M. Y. Choi, *Nanostructured, Functional, and Flexible Materials for Energy Conversion and Storage Systems*, Elsevier, 2020, pp. 1–14.
- [3] X. Yi, H. Fu, A. M. Rao, Y. Zhang, J. Zhou, C. Wang, B. Lu, *Nature Sustainability* 2024, 7, 326–337.
- [4] B. Rao, R. Francis, H. Christopher, *J. Electrochem. Soc.* 1977, 124, 1490.
- [5] M. S. Whittingham, *Science* 1976, 192, 1126–1127.
- [6] M. S. Whittingham, *J. Electrochem. Soc.* 1976, 123, 315.
- [7] Y. Huang, Y. Zhu, H. Fu, M. Ou, C. Hu, S. Yu, Z. Hu, C. T. Chen, G. Jiang, H. Gu, *Angew. Chem. Int. Ed.* 2021, 60, 4682–4688.
- [8] X. Wang, Z. Feng, X. Hou, L. Liu, M. He, X. He, J. Huang, Z. Wen, *Chem. Eng. J.* 2020, 379, 122371.
- [9] J. Xiao, J. Li, Z. Xu, *J. Hazard. Mater.* 2017, 338, 124–131.
- [10] X. Yang, C. Wang, P. Yan, T. Jiao, J. Hao, Y. Jiang, F. Ren, W. Zhang, J. Zheng, Y. Cheng, *Adv. Energy Mater.* 2022, 12, 2200197.
- [11] X. Rui, H. Tan, Q. Yan, *Nanoscale* 2014, 6, 9889–9924.
- [12] Y. Xue, T. Xu, Y. Guo, H. Song, Y. Wang, Z. Guo, J. Li, H. Zhao, X. Bai, C. Lai, *Advanced Composites and Hybrid Materials* 2024, 7, 213.
- [13] M. Abdel Maksoud, R. A. Fahim, A. E. Shalan, M. Abd Elkodous, S. Olojede, A. I. Osman, C. Farrell, A. A. H. Al-Muhtaseb, A. Awed, A. Ashour, *Environ. Chem. Lett.* 2021, 19, 375–439.
- [14] Q. Lin, S. Zhang, L.-J. Yu, B. Hou, S. Zhang, Z. Wang, J. Song, X. Zhao, *Chem. Eng. J.* 2023, 455, 140945.
- [15] D. Bhattacharjya, A. Sinhamahapatra, J.-J. Ko, J.-S. Yu, *Chem. Commun.* 2015, 51, 13350–13353.
- [16] H. Chen, J. Jiang, L. Zhang, H. Wan, T. Qi, D. Xia, *Nanoscale* 2013, 5, 8879–8883.
- [17] W. Du, Z. Zhu, Y. Wang, J. Liu, W. Yang, X. Qian, H. Pang, *RSC Adv.* 2014, 4, 6998–7002.
- [18] R. Jin, D. Liu, C. Liu, G. Liu, *RSC Adv.* 2015, 5, 84711–84717.
- [19] H. Wan, J. Jiang, J. Yu, K. Xu, L. Miao, L. Zhang, H. Chen, Y. Ruan, *CrystEngComm* 2013, 15, 7649–7651.
- [20] J. Xu, Y. Dou, Z. Wei, J. Ma, Y. Deng, Y. Li, H. Liu, S. Dou, *Adv. Sci.* 2017, 4, 1700146.
- [21] Z. Zhang, J. Zhao, M. Xu, H. Wang, Y. Gong, J. Xu, *Nanotechnology* 2018, 29, 335401.
- [22] P. Geng, S. Zheng, H. Tang, R. Zhu, L. Zhang, S. Cao, H. Xue, H. Pang, *Adv. Energy Mater.* 2018, 8, 1703259.
- [23] K. Guo, L. Bao, Z. Yu, X. Lu, *Chem. Soc. Rev.* 2024.
- [24] R. M. Bhattacharai, N. Le, K. Chhetri, D. Acharya, S. M. S. Pandiyarajan, S. Saud, S. J. Kim, Y. S. Mok, *Adv. Sci.* 2024, 11, 2308160.
- [25] C. Cong, H. Ma, *Small* 2023, 19, 2207547.
- [26] F. Wu, B. Wu, Y. Mu, B. Zhou, G. Zhang, L. Zeng, *Int. J. Mol. Sci.* 2023, 24, 6041.
- [27] J.-E. Zhou, Z. Xu, Y. Li, X. Lin, Y. Wu, A. Zeb, S. Zhang, *Coord. Chem. Rev.* 2023, 494, 215348.
- [28] X. Zhuang, S. Zhang, Y. Tang, F. Yu, Z. Li, H. Pang, *Coord. Chem. Rev.* 2023, 490, 215208.
- [29] J. Li, L. Chen, F. Wang, Z. Qin, Y. Zhang, N. Zhang, X. Liu, G. Chen, *Chem. Eng. J.* 2023, 451, 138536.
- [30] Z. Jia, D. Lan, M. Chang, Y. Han, G. Wu, *Materials Today Physics* 2023, 37, 101215.
- [31] M. Li, Y. Sun, D. Feng, K. Ruan, X. Liu, J. Gu, *Nano Res.* 2023, 16, 7820–7828.
- [32] J. Wu, Y. Chen, L. Zhang, X. Sheng, *J. Ind. Eng. Chem.* 2024, 129, 424–434.
- [33] T. Xu, Y. Wang, Z. Xiong, Y. Wang, Y. Zhou, X. Li, *Nano-Micro Lett.* 2023, 15, 6.
- [34] P. Zhou, Q. Zhu, X. Sun, L. Liu, Z. Cai, J. Xu, *Chem. Eng. J.* 2023, 464, 142508.
- [35] Y. Cui, X. Zhou, X. Huang, L. Xu, S. Tang, *ACS Appl. Mater. Interfaces* 2023, 15, 49223–49232.

- [36] Y. Xue, T. Xu, C. Wang, L. Fu, *iScience* **2024**, *27*, 110392.
- [37] Y. Jin, S. Tan, Z. Zhu, Y. He, P. Saha, Q. Cheng, *Appl. Surf. Sci.* **2022**, *598*, 153778.
- [38] L. Zhao, B. Dong, S. Li, L. Zhou, L. Lai, Z. Wang, S. Zhao, M. Han, K. Gao, M. Lu, *ACS Nano* **2017**, *11*, 5800–5807.
- [39] Y.-L. Wang, L.-Q. Fan, S.-J. Sun, J.-J. Chen, Z.-X. Wu, T.-T. Zhu, Y.-F. Huang, J.-H. Wu, *Chem. Eng. J.* **2022**, *428*, 131993.
- [40] Y. Liu, H. Xu, Y. Qian, *Cryst. Growth Des.* **2006**, *6*, 1304–1307.
- [41] X. Liu, Q. Liu, C. Chen, *Vacuum* **2021**, *183*, 109834.
- [42] T. Xiao, J. Jin, Y. Zhang, W. Xi, R. Wang, Y. Gong, B. He, H. Wang, *Electrochim. Acta* **2022**, *427*, 140851.
- [43] G. Zhou, D.-W. Wang, F. Li, L. Zhang, N. Li, Z.-S. Wu, L. Wen, G. Q. Lu, H.-M. Cheng, *Chem. Mater.* **2010**, *22*, 5306–5313.

Manuscript received: December 5, 2024
Revised manuscript received: January 7, 2025
Accepted manuscript online: January 15, 2025
Version of record online: January 27, 2025
